npj | computational materials

Article

Published in partnership with the Shanghai Institute of Ceramics of the Chinese Academy of Sciences

https://doi.org/10.1038/s41524-026-02172-0

Machine-learning discovery of extreme coherent thermal transport governed by motif-level order in Si-Ge superlattices

Shubham Tyagi[1] ✉, Julian G. Fernandez[2], Anass Sebbar[1], Natalia Seoane[3], Antonio Garcia-Loureiro[2,3] & Marc Bescond[1,4] ✉

Controlling phonon-mediated heat transport in multilayer nanostructures is central to thermal management and energy-conversion technologies. Yet identifying architectures exhibiting extreme lattice thermal conductivity (κ_l) remains challenging due to the combinatorial complexity of interface arrangements and the high computational cost of transport simulations. In superlattices, thermal transport arises from competing wave effects: coherent phonon propagation enhances transport, whereas interface scattering and localization suppress it. We study Si-Ge superlattices using an iterative machine-learning-guided non-equilibrium Green's function (NEGF) approach, where a convolutional neural network trained on NEGF data efficiently explores an experimentally constrained design space to identify both low- and high-κ_l limits. Dense interface clustering induces cumulative elastic scattering and reduces κ_l by up to 35%, while sparse, locally ordered motifs preserve extended phonon modes and enhance κ_l by up to 33% beyond periodic designs. These results are obtained at 200 K in a regime where phonon transport is predominantly coherent and elastic; thus, the identified structural trends are representative of the coherent transport regime. Our work reveals that local motif-level order, rather than global periodicity, governs extreme thermal transport in multilayer systems.

The rapid expansion of data-intensive computing, artificial intelligence, and high-performance electronics has placed unprecedented demands on thermal management at the nanoscale[1–3]. As device dimensions shrink and power densities continue to rise, heat dissipation increasingly limits performance and energy efficiency[4]. In this regime, conventional cooling strategies, such as fans, heat sinks, and liquid cooling, struggle to mitigate localized hotspots and non-uniform heat flow [3], motivating the development of materials and nanostructures with engineered thermal transport properties[5]. Because heat conduction at these length scales is dominated by lattice vibrations, controlling phonon-mediated thermal transport is a central challenge for next-generation electronics[6]. Two complementary and equally important objectives emerge in this context. On one hand, materials with suppressed lattice thermal conductivity (κ_l) are essential for thermoelectric energy conversion and active cooling, where minimizing heat leakage is critical[7,8]. Conversely, materials with enhanced κ_l are required for efficient heat spreading away from hotspots in high-power devices[9]. While extensive efforts have focused on reducing κ_l through alloying, nanostructuring, and disorder, far fewer studies have explored how both extreme suppression and enhancement of thermal transport can be achieved within a single design space composed of fixed material constituents[8]. In particular, how coherent and incoherent phonon mechanisms compete across experimentally realizable configurations remains poorly understood. Developing strategies that span both ultra-low and ultra-high κ_l within a unified framework, therefore, remains an open challenge.

Superlattices offer a versatile platform for addressing this dual objective. Periodic stacking of dissimilar materials introduces modulations in mass, bonding, and elastic properties that strongly affect phonon transport[10,11]. The interplay between coherent phonon interference and interface-induced scattering enables κ_l to be tuned over wide ranges by adjusting layer thickness and interface density[12]. Among the many superlattice systems studied to date, Si-Ge superlattices are particularly important. Owing to their structural compatibility, mature growth techniques, and relevance to CMOS technology, Si-Ge multilayers have long served as a benchmark system for exploring phonon transport phenomena and for developing thermal management strategies compatible with existing semiconductor manufacturing[13–15]. Early studies of periodic Si-Ge superlattices

[1]IM2NP, UMR CNRS 7334, Aix-Marseille Université, Paris, France. [2]Departamento de Electrónica e Computación, USC, Santiago de Compostela, Spain. [3]Centro Singular de Investigación en Tecnoloxías Intelixentes, USC, Santiago de Compostela, Spain. [4]Institute of Industrial Science, University of Tokyo, Meguro-ku, Tokyo, Japan. ✉e-mail: shubham.tyagi@im2np.fr; marc.bescond@cnrs.fr

revealed a non-monotonic dependence of κ_l on superlattice period, reflecting a crossover from incoherent, particle-like phonon transport at large periods to coherent, wave-like transport at short periods[11,16]. Subsequent work showed that graded or random layer-thickness variations can further reduce thermal transport through phonon localization[11]. These observations led to the prevailing view that increasing structural disorder generally lowers κ_l, an idea that has guided much of the design intuition for thermoelectric superlattices and multilayers.

However, this intuition does not fully capture phonon transport in complex multilayer systems. Even in globally random structures, local interface arrangements can support coherent phonon transmission over finite length scales[17]. As a result, different random configurations with identical composition and total length can exhibit vastly different thermal transport behavior [18]. Identifying interface sequences that yield extreme suppression or enhancement of κ_l is therefore challenging, particularly as the number of possible configurations grows combinatorially with system size[19]. For example, a superlattice consisting of 30 Si-Ge unit cells already corresponds to $2^{30} \approx 10^9$ distinct configurations, rendering exhaustive exploration infeasible.

Machine learning (ML) has emerged as a powerful approach for navigating high-dimensional design spaces and accelerating materials discover [20]. In thermal transport research, data-driven models have been used to predict κ_l in bulk materials, alloys, and nanostructures, and to guide the optimization of structures with target thermal properties[19,21–24]. In superlattices, ML has enabled the identification of configurations with reduced thermal conductivity[24] and, in some cases, unexpected enhancements beyond periodic references[23]. Despite these advances, many studies rely on molecular dynamics simulations, which mix elastic and inelastic scattering processes and make it difficult to isolate coherent, interference-driven phonon transport[23,25]. In addition, the use of hand-crafted descriptors or human-guided feature extraction can introduce bias and limit transferability[24]. Previous ML-assisted studies on superlattices have nevertheless demonstrated that extreme thermal conductivities can be realized by carefully tailoring the stacking sequence. For example, Bayesian optimization combined with first-principles atomistic Green's function calculations has been used to design an aperiodic GaAs/AlAs superlattice with minimal thermal conductivity[22], and a human-AI framework with hand-crafted descriptors has been applied to graphene-WS_2 heterostructures to construct interpretable ML models of thermal transport[24]. In contrast to these approaches, which either target a single optimized design in a specific material system or rely on manually engineered descriptors and empirically derived force constants, we focus here on Si-Ge superlattices in a coherent transport regime and seek an approach that both explores a large, experimentally constrained configuration space and directly links structural motifs to microscopic wave phenomena.

For superlattices dominated by elastic scattering and wave interference, an atomistic framework that explicitly captures coherent phonon transport is required. The non-equilibrium Green's function (NEGF) formalism naturally describes this regime and has been widely used to investigate coherent phonon effects, localization, and transmission spectra in multilayer systems[11,26]. This makes NEGF well-suited for investigating the fundamental mechanisms underlying extreme thermal transport in multilayers[11]. However, the high computational cost of NEGF limits its direct application to exhaustive searches over large configuration spaces, particularly when thousands of configurations must be evaluated[27]. An additional consideration arises from experimental feasibility: not all mathematically possible superlattice configurations can be realized in practice. Growth techniques impose constraints on minimum layer thickness, interface quality, and total film thickness, effectively reducing the accessible design space[28,29]. Incorporating such constraints into theoretical and computational studies is essential to ensure that predicted structures are physically meaningful and experimentally relevant.

In this work, we address these challenges by combining NEGF simulations with ML in a unified, data-driven framework to explore κ_l in Si-Ge superlattices under experimentally motivated constraints. Rather than relying on surrogate transport models or manually engineered descriptors, a convolutional neural network (CNN) is trained directly on NEGF-computed thermal conductances (σ) and derived κ_l, using encoded layer sequences that allow the model to learn spatial correlations associated with both phonon localization and enhanced coherent transmission. This approach enables an efficient exploration of the constrained design space and the identification of rare configurations exhibiting extreme thermal transport behavior that cannot be inferred from simple periodic or random limits. The results demonstrate that Si-Ge superlattices can host a remarkably wide spectrum of thermal transport responses. The remainder of the paper is organized as follows. The Results section presents and discusses the ML-guided exploration of Si-Ge superlattices. The Discussion section summarizes the main conclusions and outlook, and the Methods section describes the theoretical framework and comutational method.

Results

Thermal transport in Si-Ge superlattices

Figure 1 represents the device geometry and outlines the validation steps employed in the present study. Figure 1a shows a schematic representation of the device configuration used to model Si-Ge superlattices (Si: Green spheres and Ge: Peach spheres) within the NEGF framework, consisting of a finite device region connected to semi-infinite contacts. The semi-infinite contacts are modeled using bulk Si force constants, ensuring consistent phonon injection conditions across all configurations. Figure 1b shows the phonon dispersion of bulk Si calculated using density functional theory over the full Brillouin zone, confirming its dynamical stability. In Fig. 1c, the phonon dispersion of Si obtained from the NEGF formalism is compared with the density functional theory dispersion along the transport direction. The NEGF phonon dispersion is constructed from harmonic interatomic force constants obtained from first-principles calculations using Quantum ESPRESSO and Phonopy. The force constants are mapped onto the device geometry, Fourier-transformed in the transverse directions, and mass-normalized to form the dynamical matrix for each transverse wavevector. Diagonalization of this matrix yields the phonon dispersion, which shows excellent agreement with the corresponding first-principles results, validating the phonon transport model. For Ge, the phonon dispersion is obtained using a mass-scaling approximation in which the Si atomic mass in the dynamical matrix is replaced by the Ge mass while retaining the same harmonic force constants, following established approaches in the literature[11,30,31]. This approximation captures the dominant mass effect on phonon frequencies and has been widely validated for Si-Ge systems, allowing the Ge constituent of the superlattices to be constructed without additional first-principles calculations.

Having established the force constants and validated the phonon descriptions of the constituent materials, we next generate a large ensemble of Si-Ge superlattices and compute their thermal transport properties using the NEGF formalism. These data serve as the reference dataset for training and evaluating the ML model described in the Methods section. As discussed in the Introduction, the design space of layered Si-Ge superlattices grows combinatorially with system length, making exhaustive exploration by direct simulations infeasible.

To balance physical realism with computational tractability, we focus on superlattices with a total length of approximately 10 nm, corresponding to 20 unit cells along the transport direction. This length scale is consistent with previous theoretical and experimental studies of short-period Si-Ge superlattices and remains well within the regime accessible to coherent phonon transport simulations[32–34]. Even at this reduced length, the associated configuration space remains prohibitively large, motivating the use of ML techniques to efficiently navigate the landscape of possible layer sequences[21,23].

In order to ensure experimental relevance, additional constraints are imposed on the thicknesses of individual Si and Ge layers based on state-of-the-art epitaxial growth studies of Si-Ge heterostructures. Si layers are allowed to vary between 1 and 20 unit cells (~0.5–10 nm)[35–37], while Ge layers are restricted to 1-4 unit cells (~0.5-2 nm)[38–40]. These bounds are

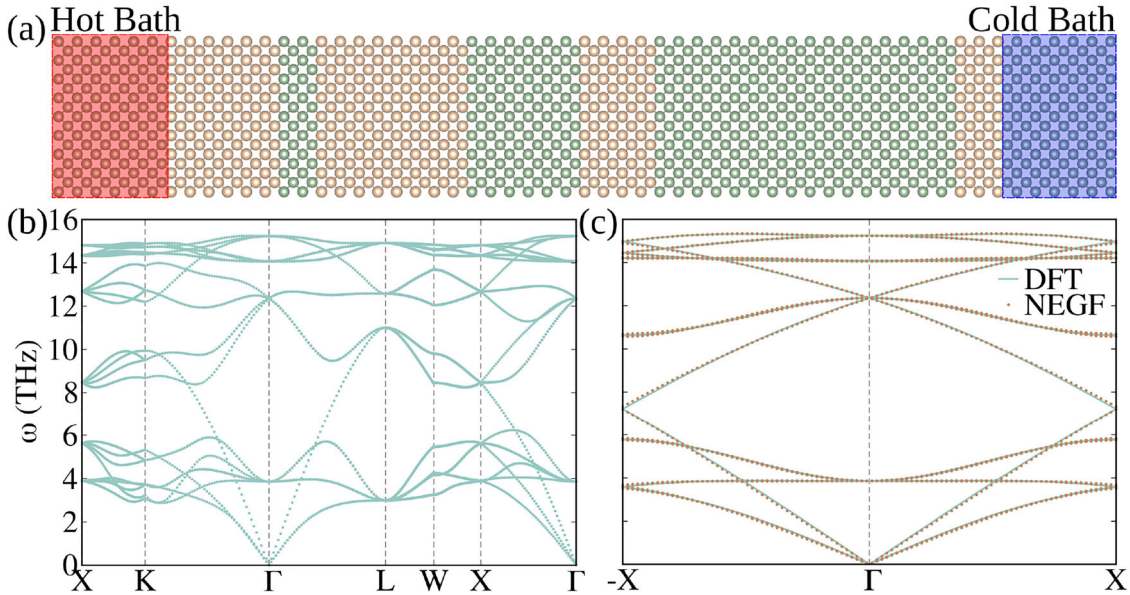

Fig. 1 | Device geometry and validation workflow employed in the study. **a** Schematic representation of the device geometry to model Si-Ge superlattices. The red and blue regions represent the contact regions. Green and peach spheres represent Si and Ge atoms, respectively. **b** Phonon dispersion of bulk Si using density functional theory over the full Brillouin zone. **c** Comparison between the phonon dispersion of bulk Si obtained from first-principles calculations and that reconstructed within the NEGF framework along the transport direction.

applied locally to each layer in the superlattice, independent of the overall stacking order.

The asymmetry between the Si and Ge thickness ranges reflects their distinct strain tolerances. For Ge grown on Si or Si-like lattices, the lattice mismatch results in a small critical thickness for coherent growth[38,41]. Experimental studies consistently show that Ge layers thicker than about 1-2 nm tend to relax via misfit dislocations or three-dimensional island formation, whereas few-monolayer Ge insertions remain coherently strained and are widely employed in short-period Si-Ge superlattices[33,40,42]. The upper bound of 4 unit cells considered here, therefore, represents an aggressive but still physically meaningful limit, approaching the onset of strain relaxation in Si-Ge heteroepitaxy[38–40].

In contrast, Si layers do not face a strict strain-driven upper thickness limit when grown on Ge or on Si-Ge stacks, and Si spacers of several nanometers are routinely realized experimentally in Si-Ge multilayer and device structures[35,36]. The primary constraint for Si instead arises at very small thicknesses: ultra-thin Si layers on Ge-rich stacks have been reported to exhibit increased roughness, waviness, or degraded superlattice periodicity, as evidenced by broadened or suppressed X-ray diffraction satellite peaks[36]. Previous studies indicate that thinner Si layers often lead to reduced structural quality, whereas thicker Si spacers yield well-defined superlattice reflections[36,37,43]. Although a minimum Si thickness of 2 unit cells would be the more conservative, experimentally safer choice, we allow Si layers down to 1 unit cell to retain sufficient structural flexibility in the modeling. Thinner Si-Ge layers could, in principle, be considered; the present bounds prioritize robustness and experimental plausibility. Applying these physically motivated local constraints substantially reduces the effective design space while preserving a wide diversity of realizable structures. For a superlattice of 20 unit cells, an unconstrained binary description would yield 2^{20} = 1, 048, 576 possible layer sequences. Imposing the above thickness bounds reduces this number to approximately 786, 568 configurations, which remains far too large for exhaustive NEGF evaluation but is sufficiently structured to enable efficient exploration using ML models.

Additional constraints could further reduce the search space, for example, by fixing the overall Si-Ge concentration or enforcing specific periodic motifs motivated by targeted experiments[29]. In the present work, however, we deliberately adopt a less restrictive approach in order to train the model on a broader and more diverse dataset, thereby improving its robustness and generalization capability. Notably, the layer-wise encoding scheme employed here (see Methods section for more details) naturally allows for finer thickness resolution, such as sub-unit-cell steps, but we restrict the present study to integer unit-cell increments to remain closely aligned with experimentally controllable growth parameters and to limit the combinatorial complexity of the dataset. Within these bounds, both periodic and random superlattice configurations are explored. Importantly, the constraints apply locally to each individual layer, rather than to the overall sequence, allowing for strongly non-uniform and random stacking orders while maintaining consistency with experimentally accessible layer thicknesses. This constrained yet highly expressive design space forms the basis for the NEGF simulations and the subsequent ML analysis presented below.

Machine-learning framework and training

Rather than assuming that the used ML model can accurately learn the full structure-property relationship from a single training step, we adopt an iterative, ML-guided workflow that explicitly targets the identification of extreme thermal transport behavior. The overall strategy, summarized in Fig. 2, begins with the generation of Si-Ge superlattice configurations within experimentally motivated constraints, which are evaluated using NEGF to form an initial training set of 800 randomly generated structures. A CNN model is trained on this data and used to efficiently screen the remaining configuration space, identifying candidates predicted to lie near the lower and upper extremes of κ_l. From each screening step, 100 extreme candidates (50 low-κ_l and 50 high-κ_l) are re-evaluated using NEGF and incorporated into the training set, after which the model is retrained and the screening process repeated. This closed feedback loop intentionally biases model refinement toward accurate identification of extreme configurations rather than uniform predictive accuracy across the entire design space. Convergence is assessed based on the stability of the NEGF-computed extreme κ_l values, consistency between ML predictions and NEGF validation, and recurrence of structurally similar extreme candidates across successive iterations. In practice, convergence is achieved once a substantial fraction of the predicted low- and high-κ_l candidates recur between iterations and the corresponding NEGF-computed κ_l values no longer change appreciably. This approach enables efficient exploration of a configuration space comprising hundreds of thousands of possible superlattice structures using a small fraction of direct NEGF evaluations,

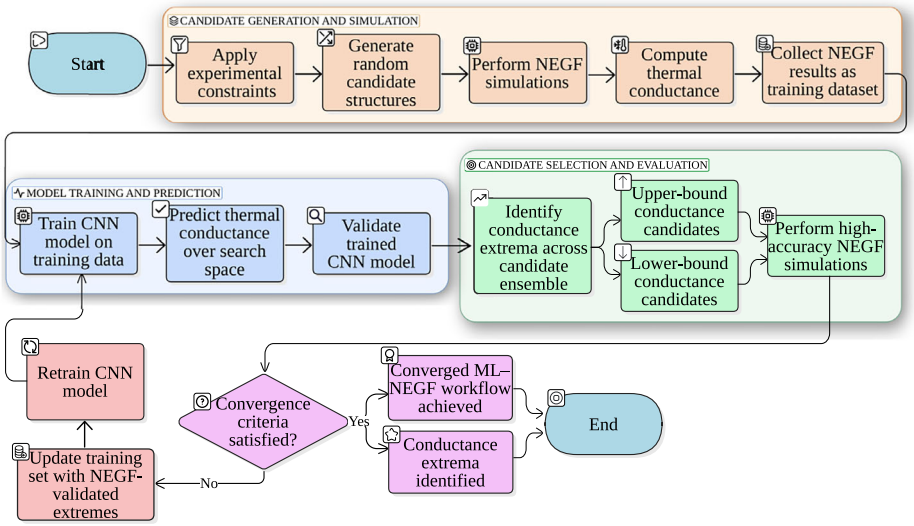

Fig. 2 | Schematic representing the NEGF-ML workflow. Convergence is achieved when NEGF stability, ML-NEGF consistency, and iterative saturation of extrema and loss are simultaneously satisfied.

thereby facilitating ML-guided discovery of extreme lattice thermal transport behavior. This ML-guided discovery approach is particularly well-suited for identifying extreme thermal transport, as structures exhibiting very low or very high κ_l constitute rare events and uniform sampling becomes statistically inefficient when each NEGF evaluation is computationally demanding. By selectively refining the surrogate model using NEGF-validated extreme candidates, the workflow concentrates computational effort where predictive accuracy is most critical, without unnecessarily improving performance in the mid-range of the distribution. Convergence in this framework does not require identical extreme candidate sets across successive iterations, since multiple configurations can exhibit nearly degenerate κ_l values and modest model updates may reshuffle candidates without altering the underlying extrema. Although the present implementation focuses on Si-Ge superlattices, the workflow itself is not material-specific. By encoding structures at the layer level and enabling the surrogate to learn interface-driven descriptors associated with coherent phonon transport and localization, the approach can be extended to other multilayer systems dominated by elastic scattering and wave interference. While the trained model remains system-dependent, the ML-guided discovery framework provides a general strategy for efficiently exploring extreme thermal transport behavior in physically constrained, high-dimensional design spaces.

To quantify structural similarity beyond exact sequence identity, each superlattice is characterized using motif-level descriptors that capture physically relevant features for thermal transport, including the total number of interfaces, statistical moments of the block-length distribution (mean, standard deviation, and maximum block length), the overall Ge fraction, and an adjacency metric defined as the mean absolute difference between consecutive block lengths. A block is defined as a continuous chain of Si or Ge unit cells. The adjacency metric captures the degree of spatial clustering of large and small regions and serves as a proxy for the correlation length of structural disorder. This representation is invariant under trivial translations of the layer sequence while remaining sensitive to variations in local arrangement that can influence transport. In addition, convergence of the iterative loop is quantified using a relative-change metric defined with respect to the immediately preceding iteration; iteration 0 serves as the initial reference and is therefore excluded from this measure. For iteration i, the relative change is defined as $\Delta\kappa_l{}^i = (|\langle\kappa_l^i\rangle - \langle\kappa_l^{i-1}\rangle|)/\langle\kappa_l^{i-1}\rangle$, where $\langle\kappa_l^i\rangle$ denotes the mean NEGF-computed κ_l of the top and bottom ten candidate structures selected in iteration i. Figure 3a shows the evolution of the relative change in κ_l together with the fraction of overlapping profiles between successive iterations. The overlap increases rapidly over the first few iterations, indicating fast localization of a relevant region of configuration space. Beyond iteration three, the overlap fraction stabilizes at a high level, reflecting repeated selection of structurally similar configurations rather than continued exploration of distinct structural regimes.

To define a practical stopping criterion for the ML-NEGF loop, we select the first iteration following the initial crossing at which the fraction of overlapping candidate profiles between successive iterations exceeds 80% and remains high in subsequent iterations (iteration 4, marked by the dashed line in Fig. 3a). This threshold reflects stabilization of the candidate set while accounting for the intrinsic degeneracy of transport-equivalent superlattice configurations. Exact 100% overlap is not expected, as structurally distinct profiles can yield nearly identical κ_l values and therefore remain indistinguishable within the chosen motif-level descriptors. Although additional iterations were performed to confirm the absence of qualitatively new candidates, no further systematic changes were observed beyond this point, and the overlap subsequently remained high. We therefore identify this iteration as the point of convergence of the learning procedure.

Discovery of extreme lattice thermal conductivity

At the converged iteration, the CNN model is used to report predictive performance metrics, as shown in Fig. 3b. The model achieves an R^2 score of at least 0.99 on both the training and validation datasets, indicating that it has learned a stable and accurate representation of the structure-property relationship within the relevant region of configuration space. Figure 3b shows a comparison between ML-predicted and NEGF-computed κ_l, together with the corresponding R^2 values. The shaded region denotes a ±5% deviation from the ideal 1:1 line, within which the majority of predictions fall. In addition, the CNN predicts κ_l with a low MAPE of 1.10% and 2.21% for training and validation sets, respectively, corresponding to an average validation RMSE of approximately 0.018 $Wm^{-1}K^{-1}$. The mean absolute error, about 0.013 $Wm^{-1}K^{-1}$, is of comparable magnitude, further confirming the quantitative agreement between ML predictions and NEGF calculations. These results demonstrate that the surrogate model achieves reliable predictive accuracy after only a few active-learning cycles. Using the converged model, we identify superlattice profiles predicted to exhibit the lowest- and highest-κ_l and subject these candidates to final NEGF validation.

Figures 4a–c and 4d–f show the three lowest- and three highest-κ_l non-degenerate ML predicted profiles, respectively. The corresponding NEGF-computed κ_l values are 0.378, 0.423, 0.436, 1.848, 1.477, 1.356 $Wm^{-1}K^{-1}$, respectively, all lying within the predefined accuracy bounds of the ML model. These results immediately demonstrate that interface density alone is a necessary but insufficient descriptor of thermal transport. Among the three lowest-κ_l configurations, κ_l varies by nearly 15% despite identical interface counts and identical Si-Ge composition, indicating that the spatial distribution and clustering of interfaces play a decisive role. Similarly, in the

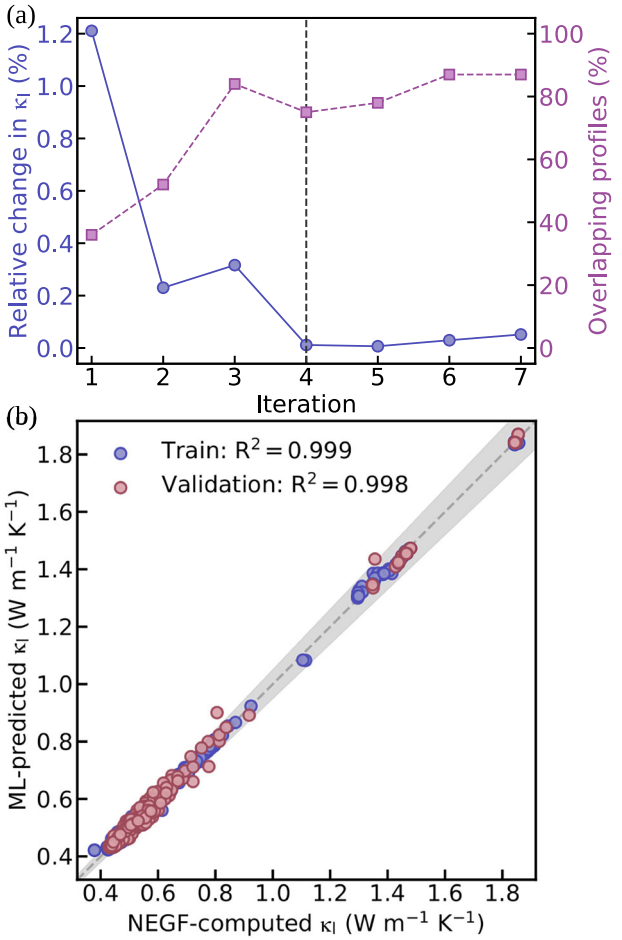

Fig. 3 | Convergence and predictive performance of the ML-NEGF framework. **a** Relative change in κ_l and fraction of overlapping profiles as a function of iteration in ML-NEGF loop. **b** Comparison of ML-predicted and NEGF-computed κ_l for the ML corresponding to iteration 4 (dashed line in (**a**)). The dashed gray line in (**b**) denotes the ideal 1:1 correspondence. The shaded region represents a fixed ± 5% deviation from this line and is shown as a visual guide to highlight agreement between ML predictions and NEGF results.

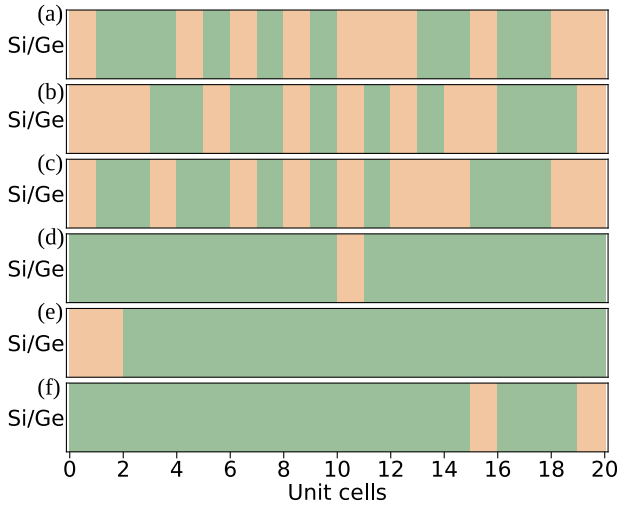

Fig. 4 | ML-identified superlattice profiles spanning the lattice thermal conductivity range. Superlattice profiles corresponding to the **a–c** lowest- and the **d–f** highest-κ_l values identified by the ML-NEGF framework.

high-κ_l regime, while low Ge fraction and sparse interfaces are necessary to achieve large κ_l, they are not sufficient to uniquely determine transport behavior. Notably, the ML predicted high-κ_l configurations are simple but not trivially equivalent to periodic superlattices. Contrary to the common expectation that deviations from strict periodicity universally suppress coherent transport, these structures preserve high transmission despite broken global periodicity. Rather than identifying a single optimal design, the ML model learns a low-dimensional manifold of transport-equivalent configurations governed by motif-level descriptors, explaining the observed degeneracy in both the low- and high-κ_l regimes. Closer inspection of the high-κ_l configurations reveals a weak but systematic dependence on Ge block placement. For profiles with identical Ge fraction and interface count, κ_l varies monotonically with the spatial position of the Ge block, attaining maximal values when the Ge region is located near the device boundaries or center. Shifting the same block away from these locations produces a small but reproducible reduction in κ_l, while fragmenting the block into multiple segments further suppresses transport. This hierarchy reflects second-order sensitivity to boundary coupling and internal reflections, highlighting that ML captures not only dominant motif-level descriptors but also subtle spatial effects beyond simple interface counting. While bulk Si trivially maximizes κ_l and remains fully CMOS compatible, it offers no internal tunability for thermal transport engineering beyond geometry and size effects. In contrast, Si-Ge superlattices provide a technologically mature, CMOS-compatible, and experimentally accessible platform in which κ_l can be continuously engineered through interface design without changing the underlying material system. This capability enables independent control of thermal transport while preserving electronic compatibility, making Si-Ge superlattices directly relevant for nanoscale thermal management, thermoelectrics, and phononic device engineering.

In the low-κ_l regime, most identified configurations cluster around high interface density, short and nearly uniform block lengths (mean block size ~1.5 unit cells), and near-equiatomic composition. Within this search space, κ_l varies primarily with the spatial adjacency metric, indicating that transport suppression is governed by cumulative weak elastic scattering distributed across many interfaces rather than resonant, site-specific localization at isolated regions. In contrast, the high-κ_l regime is characterized by sparse interfaces, long contiguous Si blocks, and low Ge fraction, with residual sensitivity arising mainly from contact coupling and mode injection rather than bulk scattering. Degeneracy in the low-κ_l regime is therefore disorder-driven, whereas quasi-degeneracy in the high-κ_l regime reflects coherent transport constrained by boundary effects.

To place these ML predicted extremes in a broader physical context, we compare them against intuitive reference designs. Although these reference designs do not strictly satisfy all experimental constraints imposed in the present study, they represent the best physically motivated benchmarks available; comparison with constraint-matched reference structures would further underline the advantage of the ML predicted configurations. For the low-κ_l case, we consider a graded Si-Ge superlattice, commonly employed to introduce controlled disorder. Owing to the fixed system length of 20 unit cells, only a single graded configuration with increasing layer thicknesses (1-2-3 unit cells per period) can be constructed (Fig. 5a). NEGF calculations yield κ_l of 0.573 $Wm^{-1}K^{-1}$ for this structure. For the high-κ_l comparison, we examine all distinct periodic Si-Ge superlattices compatible with the same system length (Figs. 5c–f). Among these, the maximum κ_l is 1.393 $Wm^{-1}K^{-1}$ of Fig. 5c. Relative to these benchmarks, the ML predicted lowest-κ_l configuration achieves a 35% reduction compared to the graded reference, while the highest-κ_l configuration exhibits a 33% enhancement over the best periodic design. Previous studies have reported only modest improvements of ~ 3% over periodic superlattices over periodic superlattices[23]; the present results demonstrate that our ML-guided exploration can uncover non-intuitive configurations that substantially expand the achievable bounds of thermal transport.

To assess whether the reduced κ_l of ML predicted low-κ_l configurations arises solely from increased interface density compared to graded superlattice, we construct a series of intuitive "fragmented graded" reference

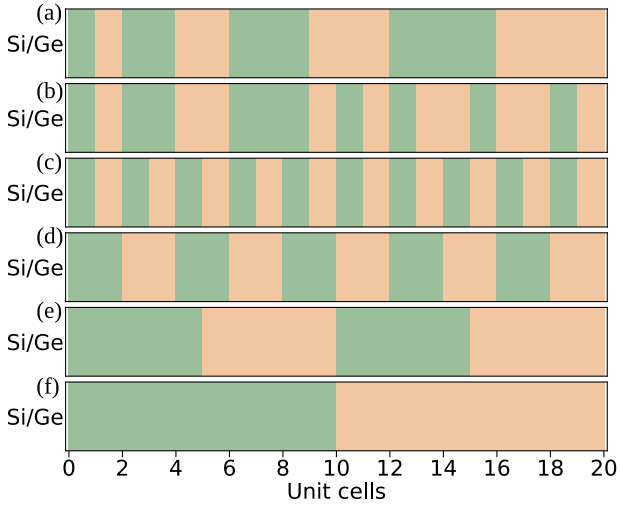

Fig. 5 | Intuitive reference superlattice profiles for comparison. a Lowest (graded), **b** fragmented graded and **c**–**f** highest (periodic) κ_l value profiles.

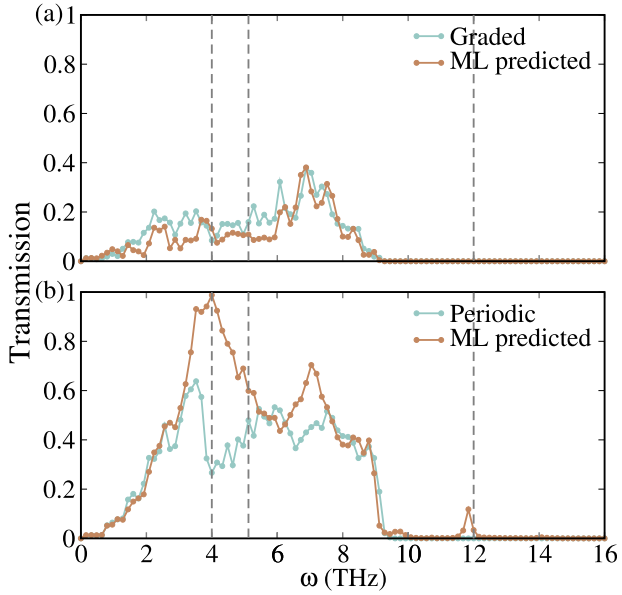

Fig. 6 | Transmission characteristics of ML-identified and reference superlattice configurations. Transmission as a function of frequency for **a** the lowest-κ_l case, comparing the ML-identified configuration with the graded reference, and **b** the highest- κ_l case, comparing the ML-identified configuration with periodic reference superlattices. Vertical dashed lines indicate the frequencies selected for phonon-density analysis.

designs with matched interface count, composition, and total length. These 'fragmented graded' configurations are obtained by subdividing the graded superlattice while preserving its overall material fraction. Although these structures introduce additional interfaces and further reduce κ_l relative to the original graded design, they do not achieve the broadband transmission suppression observed in the ML predicted configurations. The best fragmented graded structure (Fig. 5b) yields κ_l of 0.466 $Wm^{-1}K^{-1}$, approximately 23% higher than the ML predicted minimum. An analogous comparison in the high-κ_l regime, using structures with matched interface counts, likewise confirms that interface density alone cannot explain the observed transport extremes.

Importantly, the ML-guided approach does not identify a single optimal structure but rather maps out entire families of transport-equivalent configurations, providing both flexibility and robustness for practical superlattice design. To further elucidate the microscopic transport mechanisms underlying these motif-level trends, we analyze the phonon transmission spectra and PR of the ML-predicted extreme configurations and compare them against intuitive periodic and graded reference structures. These spectral quantities provide complementary insight into how structural motifs influence mode propagation, coherence, and spatial localization within the transport regime.

Analysis of phonon characteristics

Within the NEGF framework, phonon transmission quantifies the ability of vibrational modes at a given frequency to propagate coherently across the superlattice and couple to the contacts, while the PR characterizes the spatial extent of these modes within the device. Although related, these quantities probe distinct aspects of phonon transport: transmission reflects coherent propagation and contact coupling, whereas PR distinguishes extended modes from spatially confined or quasi-localized vibrations. Figures 6a and 6b show the phonon transmission spectra for the ML predicted extreme configurations, compared with graded and periodic reference superlattices. In the lowest-κ_l regime, the ML predicted structure exhibits a broad suppression of transmission across the dominant heat-carrying frequency window, exceeding that of the graded reference over most frequencies. The accumulation of many weak elastic reflections, each insufficient to localize a mode individually, but collectively suppresses transmission. As seen in Fig. 6a, the low-frequency transmission of the ML-predicted low-κ_l configuration is only moderately reduced compared to the graded reference, reflecting the fact that the graded structure already strongly suppresses coherent transport in this regime. The additional reduction in κ_l therefore arises mainly from stronger suppression in the low- to mid-frequency range (~2–6 THz) and from the integrated effect over the full spectrum. Consistent with the comparison in the Results section, this spectral difference corresponds to a ~35% decrease in κ_l relative to the graded reference (from 0.573 to 0.378 $Wm^{-1}K^{-1}$ for the ML-predicted low-κ_l configuration). In contrast, in the highest-κ_l regime, the ML predicted configuration maintains high transmission over a wide low-frequency range, closely resembling or exceeding the best periodic reference despite subtle deviations from strict periodicity.

The corresponding PRs (Fig. 7a, b) provide complementary insight into the spatial character of the vibrational modes. Frequency ranges associated with suppressed transmission are often accompanied by reduced PR, particularly in non-periodic configurations where multiple interfaces disrupt phase coherence and induce partial spatial confinement of vibrational energy. In the lowest-κ_l ML configurations, transmission remains consistently lower than in the graded reference across much of the transport window, yet the PR follows a similar frequency dependence and remains comparatively moderate over a broad frequency range. This indicates that vibrational modes are not strongly localized at a single interface or compositional transition. Instead, the modes remain spatially extended while experiencing distributed confinement across multiple interfaces. Transport suppression therefore, originates from the cumulative effect of many weak elastic reflections, each insufficient to localize a mode individually but collectively reducing net transmission. This behavior is consistent with distributed elastic scattering rather than resonant, site-specific localization. In contrast, periodic reference structures exhibit frequency regions where transmission is strongly reduced even while the PR remains moderate. The broad high-PR regions observed in ML's highest-κ_l configuration indicate vibrational modes that remain spatially extended across the entire device. In this regime, phonon amplitudes are distributed over most atoms rather than confined to specific interfaces. Since the PR directly reflects the spatial extent of vibrational modes, the persistence of moderate PR values indicates that transport suppression in the periodic configuration compared to highest-κ_l ML configuration does not originate from spatial localization. Rather, it arises from coherent interference and elastic reflection acting on spatially extended phonon modes. While spatial localization itself is a consequence of coherent interference, it requires persistent destructive interference leading to wavefunction confinement, which is not observed here. The observed reduction in transmission is therefore attributed either to interference-

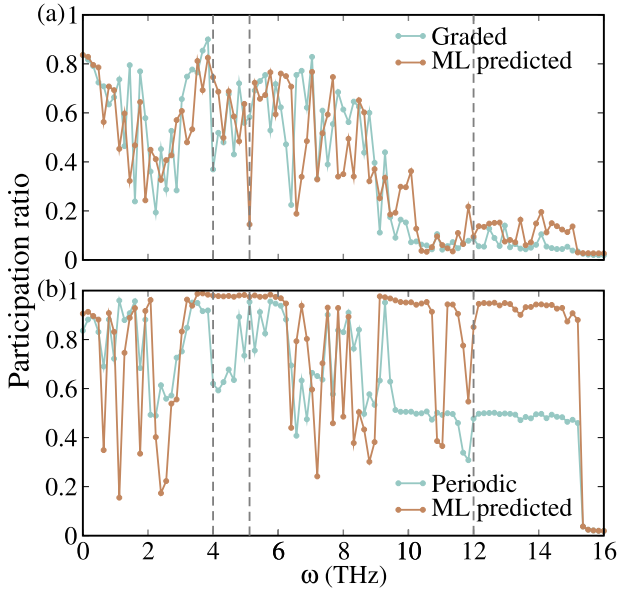

Fig. 7 | Phonon participation ratio of ML-identified and reference superlattice configurations. Participation ratio as a function of frequency for **a** the lowest-κ_l case, comparing the ML-identified configuration with the graded reference, and **b** the highest- κ_l case, comparing the ML-identified configuration with periodic reference superlattices. Vertical dashed lines indicate the frequencies selected for phonon-density analysis.

induced reflection of extended modes (periodic case) or to the cumulative effect of multiple weak elastic reflections distributed across many interfaces (ML lowest-κ_l case).

To further elucidate the microscopic origin of these trends, we examine the spatial distribution of phonon density at representative frequencies selected to capture (i) highly transmitting modes and high PR, (ii) transport-limiting frequencies with low PR, specifically for low-κ, and (iii) high-frequency modes with negligible transmission. The corresponding frequencies are represented by a dashed line in Figs. 6 and 7. Figure 8a and b show the phonon density at $\omega \approx 4$ THz, corresponding to a dominant heat-carrying frequency. At this frequency, the ML predicted low-κ_l configuration exhibits a spatially distributed phonon density without strong site-specific localization, indicating that vibrational modes remain extended across the superlattice. In contrast, the graded reference structure shows pronounced spatial localization of phonon density near specific compositional transition regions (single block marked by dashed lines and shaded region), indicative of resonant trapping of vibrational modes, consistent with previous observations[11]. Despite these qualitative differences in mode character, transmission at this frequency remains finite, indicating that $\omega \approx 4$ does not dominate the overall suppression of κ_l in the ML predicted configurations. For the high-κ_l regime at the same frequency, the ML-identified configuration displays a nearly uniform phonon density throughout the system, consistent with fully extended propagating modes and the near-unity transmission observed in Fig. 6b. By comparison, the periodic reference already exhibits strong spatial modulation of phonon density, reflecting coherent interference and partial elastic reflection despite the absence of strong localization. This behavior explains why periodic structures exhibit reduced transmission relative to the ML predicted high-κ_l configurations even when participation ratios remain high.

At a transport-limiting frequency $\omega \approx 5.12$ THz (Fig. 8c, d), the distinction between graded and ML predicted low-κ_l configurations becomes

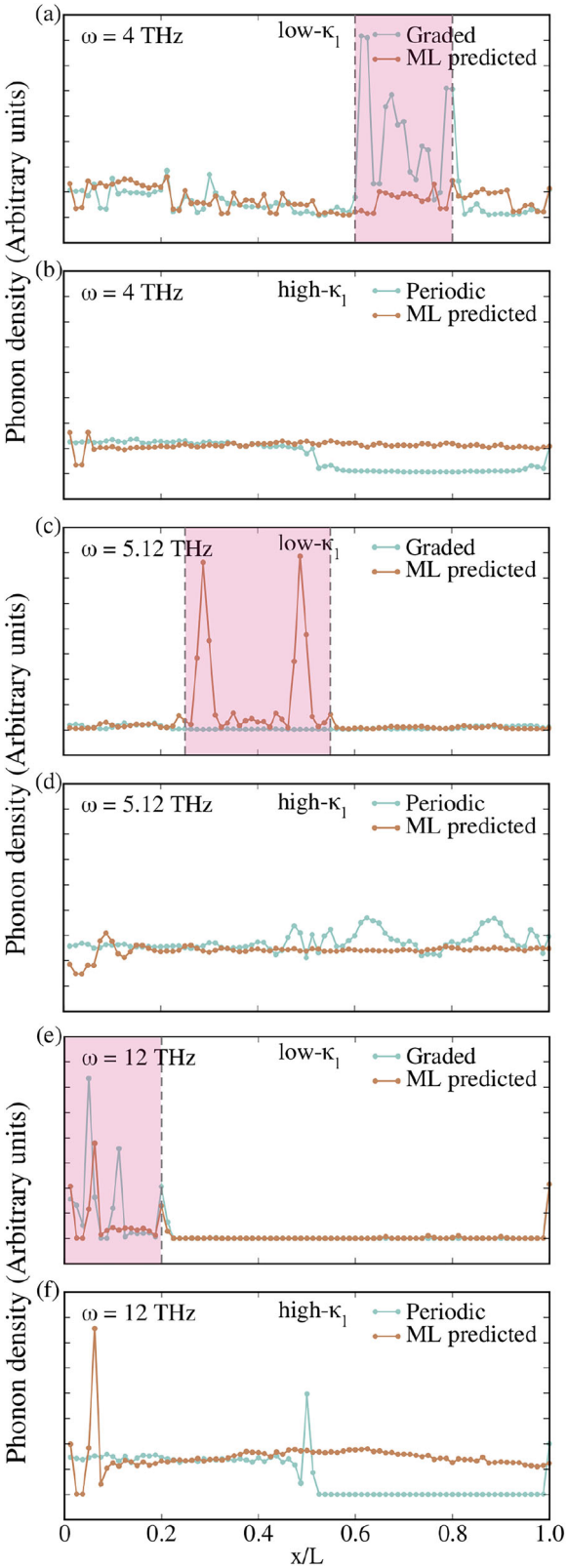

Fig. 8 | Phonon density for ML predicted extreme configurations and reference structures at representative frequencies. Phonon density at ω of (**a**, **b**) 4 THz (**c**, **d**) 5.12 THz, and (**e**, **f**) 12 THz. Shaded regions highlight the localization of vibrational energy in the graded configurations.

Table 1 | Structural descriptors and thermal conductivity for representative low- and high-κ_l Si-Ge superlattices

Configuration	Interfaces	Mean	Std.	Max	Adjacency	Ge frac.	Ge asymmetry	κ_l (W $m^{-1}K^{-1}$)	NEGF observables
ML-low 1	12	6.15	2.98	12	3.00	0.50	+ 0.10	0.378	Cumulative elastic scattering with distributed confinement; suppressed mid-ω transmission; low PR
ML-low 2	12	6.15	2.98	12	2.67	0.50	0.00	0.423	Cumulative elastic scattering with distributed confinement; suppressed mid-ω transmission; low PR
ML-low 3	12	6.15	2.98	12	2.33	0.50	+ 0.10	0.436	Cumulative elastic scattering with distributed confinement; suppressed mid-ω transmission; low PR
ML-high 1	2	26.67	16.11	40	34.00	0.05	− 0.05	1.848	Robust propagation with weak elastic reflection; high broadband transmission, high PR
ML-high 2	2	40.00	32.00	72	64.00	0.10	+ 0.10	1.477	Robust propagation with weak elastic reflection; high broadband transmission, high PR
ML-high 3	3	20.00	23.32	60	24.00	0.10	− 0.10	1.356	Robust propagation with weak elastic reflection; high broadband transmission, high PR

The structural metrics correspond to the motif-level descriptors defined to quantify structural similarity (mean, standard deviation, maximum block length, adjacency, and Ge fraction) for Fig. 3a. In addition, we include a spatial Ge asymmetry, defined as the difference between the number of Ge layers in the left and right halves of the superlattice, normalized by the total number of unit cells. We also examined the Ge center-of-mass position and block-sequence entropy as candidate descriptors; while these carry equivalent structural information, Ge asymmetry provides the most direct connection. The descriptors are evaluated on the discretized layer representation of the superlattice (each unit cell is discretized into four atomic layers; see Methods section for more details).

pronounced. In graded structures, phonon density does not exhibit strong localization at this particular frequency, consistent with the relatively high PR value observed in Fig. 7a. In contrast, the ML predicted low-κ_l configuration exhibits confinement that extends over multiple blocks rather than being pinned to a single interface or block (marked by dashed lines and shaded region). The phonon density is attenuated over a broad spatial region, indicating distributed confinement arising from the accumulation of many weak elastic reflections rather than resonant trapping. In this regime, no single interface dominates phonon confinement; instead, transport is suppressed through the collective effect of repeated partial reflections throughout the superlattice. This mechanism explains the broadened transmission suppression and lower integrated κ_l achieved by the ML predicted structures relative to graded designs. The ML predicted high-κ_l configurations show behavior qualitatively similar to periodic superlattices, maintaining extended phonon density profiles consistent with efficient transport and high PR.

Finally, at higher frequencies ($\omega \geq 10$ THz (12 THz); Fig. 8e, f), transmission vanishes for all structures while participation ratios remain finite, confirming the presence of vibrational modes that are spatially extended within the device but are poorly coupled to the contacts and therefore do not contribute appreciably to thermal transport. This decoupling highlights the necessity of combining transmission, participation ratio, and phonon density analyses to fully characterize thermal transport. Taken together, these results demonstrate that extreme thermal transport in Si-Ge superlattices arises from distinct wave-based microscopic mechanisms: coherent interference and elastic reflection in periodic structures, resonant localization in graded designs, cumulative elastic scattering with distributed confinement in ML predicted low-κ_l configurations, and robust propagation of extended modes with weak elastic reflection in ML predicted high-κ_l configurations.

Motif-level ordering

To summarize the joint influence of motif-level descriptors and the associated microscopic transport mechanisms, Table 1 lists three representative low- and high-κ_l configurations together with their descriptor values and qualitative NEGF signatures. The low-κ_l structures systematically exhibit high interface density, short mean block lengths, moderate block-length variance, and near-equiatomic Ge fraction, which correlate with reduced mid-frequency transmission, low participation ratio, and distributed confinement of phonons. By contrast, high-κ_l structures have few interfaces, long blocks, and low Ge fraction, and display high transmission, high PR, and extended vibrational modes. These trends highlight that extreme thermal conductivities arise from a cooperative interplay of composition, interface density, and block-length statistics, rather than from any single factor alone. Crucially, within the low-κ_l class, where interface count, mean block length, and Ge fraction are identical across all three configurations, it is the adjacency index that differentiates their conductivities, reflecting the sensitivity of phonon scattering to the sequential ordering of block lengths beyond their marginal statistics. Similarly, the Ge asymmetry index distinguishes the high-κ_l configurations, capturing the spatial distribution of the Ge sublattice and its directional influence on phonon transmission. We note that, within the experimentally constrained design space explored here, all CNN-identified low-κ_l extrema are near-equiatomic (Ge fraction ~0.5); for structures with comparable interface density and short blocks but Ge fractions significantly different from 0.5 (not shown in Table 1), the thermal conductivity is consistently higher. This indicates that near-equiatomic composition is favorable but must act together with high interface density and appropriate block-length patterns to achieve the lowest conductivities.

Discussion

In this work, we introduced an ML-guided NEGF framework for the targeted discovery of extreme κ_l in Si-Ge superlattices. By iteratively coupling first-principles transport calculations with a 1D-CNN, we efficiently navigated a large, experimentally constrained configuration space and converged on structurally distinct profiles exhibiting extreme thermal transport behavior. All simulations were performed at 200 K, where phonon transport in the studied systems is expected to be dominated by coherent, elastic processes, so the main conclusions concern how structure controls coherent thermal transport. At higher operating temperatures, anharmonic phonon-phonon scattering will reduce coherence and quantitatively renormalize the thermal conductivity, but the underlying structure-transport relationships identified here are expected to remain qualitatively unchanged. Using this approach, we identify superlattice configurations whose κ_l exceeds that of the best periodic reference by approximately 33%, substantially surpassing the ~ 3% enhancement reported in prior studies[23]. Conversely, we discover configurations with κ_l reduced by approximately 35% relative to graded superlattices, which are commonly regarded as near-optimal disorder-engineered structures. These results establish that both the upper and lower bounds of thermal transport in Si-Ge superlattices extend well beyond those accessible through conventional periodic or graded design strategies. Beyond identifying extreme values, our analysis reveals that κ_l is governed by a small set of motif-level descriptors, interface density, block-length statistics, and spatial clustering, leading to broad degeneracy in both low- and high-κ_l regimes. Distinct atomic-scale profiles can therefore exhibit nearly identical transport properties, underscoring the limitations of structure-by-structure intuition and highlighting the importance of learning-based exploration.

A combined analysis of phonon transmission, participation ratio, and phonon density elucidates the microscopic mechanisms underlying these

extremes. Low-κ_l configurations suppress transport through cumulative elastic scattering across many closely spaced interfaces rather than through strong localization at isolated regions, while high-κ_l configurations support extended, weakly reflected modes with minimal sensitivity to interface placement. This distinction explains both the observed degeneracy and the robustness of the ML-predicted optima. This distributed confinement mechanism contrasts sharply with the resonant, site-specific localization observed in graded structures and explains why ML-predicted designs can surpass intuitive disorder-engineering strategies. These findings indicate that minimizing κ_l in the ballistic regime does not require strong localization at isolated sites, but rather the suppression of coherent phonon transmission across a broad frequency window through distributed elastic scattering.

Overall, this study demonstrates that ML can serve not merely as a surrogate model but as a discovery tool that exposes hidden design principles and expands the achievable bounds of thermal transport. The proposed workflow is general because it relies only on layer-resolved structural encoding, physics-based transport labels, and iterative model refinement, without invoking material-specific or hand-crafted descriptors. As a result, it can be readily extended to other material systems, heterostructures, and transport regimes, providing a scalable pathway for the inverse design of thermal materials beyond human intuition.

Methods

First-principles simulations

For material properties of Si, we perform first-principles calculations based on density functional theory within the generalized gradient approximation using Perdew-Burke-Ernzerhof for the exchange-correlation functional, as implemented in the Quantum-ESPRESSO code [44]. A plane-wave energy cutoff of 60 Ry is employed, and the Brillouin zone is sampled using a Monkhorst-Pack 8 × 8 × 8 k-point mesh. The total energy is converged to within 10^{-8} Ry, and structural relaxation is carried out until the Hellmann-Feynman forces on all atoms are below 10^{-6} Ry/bohr. To compute the harmonic force constants, a 3 × 3 × 3 supercell is constructed, and the finite-displacement method is applied using Phonopy [45]. The Brillouin zone of the supercell is sampled with a Monkhorst-Pack 3 × 3 × 3 k-point grid. Following previous studies, the harmonic force constants of Ge are approximated to be identical to those of Si, with only the difference in atomic mass taken into account [11,30,31].

Quantum transport simulations

The σ and the derived κ_l calculations are performed in the framework of the NEGF method, implemented in the in-house developed tool [11,31]. The harmonic force constants generated using a combination of Quantum ESPRESSO and Phonopy serve as the input to the NEGF tool. To describe heat transport in the device region via phonons, we describe retarded Green's function as:

$$G^R(\omega; q_t) = \left[\omega^2 I - \widetilde{\Phi}(q_t) - \Sigma^R(\omega; q_t)\right]^{-1}, \tag{1}$$

where I is the identity matrix, ω is the phonon frequency, and q_t denotes the wave vector along the transverse periodic plane. The matrix $\widetilde{\Phi}(q_t)$ represents the Fourier-transformed harmonic force constant matrix, and Σ^R is the retarded self-energy accounting for the coupling between the device region and the contacts [46,47]. The retarded self-energy is obtained from the surface Green's functions of the semi-infinite leads using the decimation technique[48] and is expressed as:

$$\Sigma^R(\omega; q_t) = \Sigma_1^R(\omega; q_t) + \Sigma_2^R(\omega; q_t), \tag{2}$$

The greater and lesser Green's functions are evaluated as [47,49]:

$$G^{>,<}(\omega; q_t) = G^R(\omega; q_t)\,\Sigma^{>,<}(\omega; q_t)\,G^A(\omega; q_t), \tag{3}$$

where G^A is the advanced Green's function, given by the Hermitian conjugate of G^R. The greater and lesser self-energies include only the contributions from the two contacts,

$$\Sigma^{>,<}(\omega; q_t) = \Sigma_1^{>,<}(\omega; q_t) + \Sigma_2^{>,<}(\omega; q_t), \tag{4}$$

and are determined by the Bose-Einstein distributions of the contacts and the corresponding retarded self-energies.

The σ is then obtained using the Landauer formula[50] as:

$$\sigma = \frac{1}{A}\int \frac{\hbar\omega}{N}\sum_{q_t} \mathrm{Tr}\left[\Gamma_1(\omega; \mathrm{q_t})\,\mathrm{G^R}(\omega; \mathrm{q_t})\,\Gamma_2(\omega; \mathrm{q_t})\,\mathrm{G^A}(\omega; \mathrm{q_t})\right] \times \frac{\partial f_{\mathrm{BE}}(\omega, T)}{\partial T}\, d\omega, \tag{5}$$

where A is the transverse cross-sectional area, f_{BE} denotes the Bose-Einstein distribution function, Tr represents the trace of a square matrix, and N is the number of transverse wave vectors. The coupling matrices $\Gamma_{1(2)}$ are defined as $\Gamma_{1(2)} = i\left(\Sigma^R_{1(2)} - \Sigma^A_{1(2)}\right)$ where the advanced contact self-energy Σ^A is the Hermitian conjugate of the retarded self-energy Σ^R. The κ_l is then derived from σ using device length L as $\kappa_l = \sigma$L. The phonon density is calculated using the diagonal of $G^>$ as [51]:

$$\rho(\omega, R_n) = \mathrm{Tr}\left[\frac{1}{N}\sum_{q_t} iG^<_{nn}(\omega; q_t)\right] \times \frac{\omega}{\pi}, \tag{6}$$

where R_n denotes the position of atomic site n.

To characterize phonon localization, we compute the phonon participation ratio (PR)[22,52], defined as:

$$\mathrm{PR}(\omega) = \frac{[\Sigma_n \mathrm{LDOS}(\omega, R_n)]^2}{N_a \Sigma_n [\mathrm{LDOS}(\omega, R_n)]^2}, \tag{7}$$

where N_a is the total number of atoms in the device and $\mathrm{LDOS}(\omega, R_n)$ is the local density of states at frequency ω. The local density of states is evaluated as

$$\mathrm{LDOS}(\omega, R_n) = \frac{\omega}{\pi} \times \frac{1}{N}\sum_{q_t} i\left[G^>_{nn}(\omega; q_t) - G^<_{nn}(\omega; q_t)\right], \tag{8}$$

where n labels the atomic site.

A frequency grid consisting of 200 points is used for the phonon energy integration, and the transverse direction is sampled using an $N = 15 \times 15$ q_t-point mesh, as determined from convergence tests. Throughout this work, all simulation results are presented at a temperature of 200 K. This choice is motivated by previous studies showing that, at this temperature, anharmonic phonon-phonon scattering is significantly suppressed, allowing phonon transport to be dominated by elastic processes[11,31]. As a result, wave effects such as phonon coherence and localization can be more clearly observed while minimizing the influence of inelastic scattering mechanisms. Although our calculations are restricted to 200 K, we expect the qualitative structural trends identified here to persist at higher temperatures. Prior anharmonic-phonon NEGF studies of Si-Ge-type interfaces have shown that including three-phonon scattering enhances the thermal boundary conductance by only about 10% at room temperature and up to ~20% at 600 K compared with the harmonic limit, while the overall spectral features of heat transport remain essentially unchanged [31]. This smooth, moderate renormalization with temperature suggests that anharmonic phonon-phonon scattering primarily rescales the magnitude of thermal transport, rather than altering the underlying wave-based mechanism set by geometry and coherent scattering. From this perspective, the ballistic NEGF results at 200 K provide a coherent-transport baseline, and the structure-transport relationships identified here

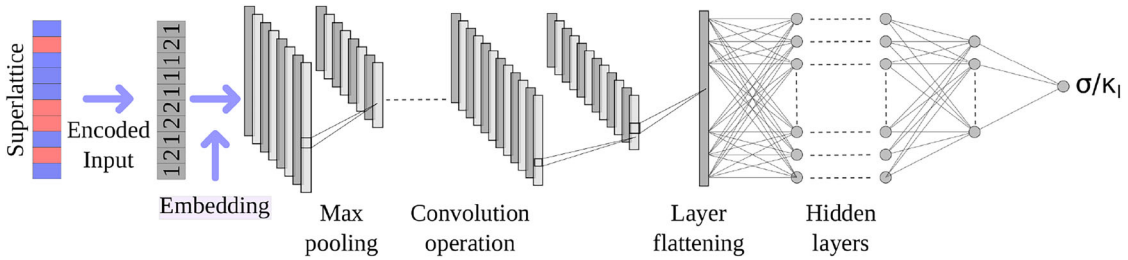

Fig. 9 | Schematic representation of the 1D-CNN model used in this study. 1D convolutional and pooling layers extract local structural features, which are subsequently processed by fully connected layers to predict the σ/κ_l. The CNN surrogate is used within an iterative ML-NEGF framework, as described in the text.

are expected to remain qualitatively valid at elevated temperatures, even though their quantitative impact will be reduced by increased decoherence.

Machine learning workflow

We employ a one-dimensional CNN (1D-CNN) to predict the σ and the corresponding κ_l from the atomic-scale description of Si-Ge superlattice structures. A schematic illustration of the network architecture is shown in Fig. 9. The input to the model is a structural representation consisting of 20 Si-Ge unit cells along the transport direction. Each unit cell is discretized into four atomic layers, resulting in a 1D sequence of 80 layers. Each layer is encoded using an integer label, where 1 and 2 represent Si and Ge, respectively. This fine-grained layer-wise encoding provides additional flexibility to represent sub-unit-cell variations, such as half-unit-cell modifications or interface reconstructions, if required.

Before being processed by the CNN, the discrete input sequence is mapped to a continuous vector representation using an embedding layer of dimension 8. This embedding allows the network to avoid artificial ordinal relationships between Si and Ge [53]. The embedded sequence is then passed through a series of 1D convolutional layers designed to extract local structural motifs and interface features relevant to phonon transport. The number of convolutional layers, the number of filters per layer, and the kernel sizes are treated as hyperparameters and optimized during model selection. Specifically, we consider 3 convolutional layers, with the number of filters ranging from 36 to 60 and kernel sizes between 3 and 7. Rectified Linear Unit (ReLU) activation functions are used after each convolution to introduce nonlinearity.

To reduce the spatial dimensionality and improve translational invariance, max-pooling layers are applied after every two convolutional layers. Early stopping based on the validation loss is employed to prevent unnecessary training once convergence is reached. All network weights are initialized using a random initialization scheme consistent with the ReLU activation. Following the convolutional feature extraction, the resulting feature maps are flattened and passed to a fully connected neural network. This dense network consists of 2 hidden layers with 512 neurons per layer, each followed by ReLU activation. Dropout regularization, with a dropout rate of 0.25, is employed after the hidden layer to mitigate overfitting. The final output layer consists of a single neuron with linear activation, corresponding to the predicted value of σ (or κ_l). The model is trained by minimizing the mean squared error (MSE) loss between the ML-predicted values and the reference values obtained from NEGF calculations. For a training set consisting of N_s samples, the MSE is defined as:

$$MSE = \frac{1}{N_s}\sum_{i=1}^{N_s}\left(y_i^{NEGF} - \hat{y}_i^{ML}\right)^2. \tag{9}$$

The performance of the trained models is evaluated using multiple regression metrics, including the coefficient of determination (R^2), root mean square error (RMSE), and mean absolute percentage error (MAPE). With reference values y_i, mean of the reference values $\bar{y}$, and predicted values $\hat{y}_i$, these metrics are defined as

$$R^2 = 1 - \frac{\sum_{i=1}^{N_s}\left(y_i - \hat{y}_i\right)^2}{\sum_{i=1}^{N_s}\left(y_i - \bar{y}\right)^2}, \tag{10}$$

$$\mathrm{RMSE} = \sqrt{\frac{1}{N_s}\sum_{i=1}^{N_s}\left(y_i - \hat{y}_i\right)^2}, \tag{11}$$

and

$$\mathrm{MAPE} = \frac{1}{N_s}\sum_{i=1}^{N_s}\left|\frac{y_i - \hat{y}_i}{y_i}\right| \times 100\%. \tag{12}$$

The CNN is trained using an 80/20 stratified train-validation split of the NEGF dataset, and all reported performance metrics refer to the held-out validation set. To assess robustness, we retrained the model with four different random seeds, which affect both weight initialization and data shuffling, and also varied the initial random batch of structures used to start the active-learning loop. In all cases, the validation R^2 exceeded 0.99 and the predicted low- and high-κ_l extrema differed by less than 1% in κ_l compared to the reference run, while exhibiting the same qualitative structural characteristics (interface density, block-length statistics, and composition). These tests indicate that the CNN predictions, and in particular the identified extreme-thermal-conductivity configurations, are robust with respect to random initialization and data partitioning.

Data availability

The datasets generated and/or analyzed during the current study are not publicly available due to their large size and ongoing related studies, but are available from the corresponding author on reasonable request.

Received: 12 March 2026; Accepted: 26 May 2026;
Published online: 04 June 2026

References

1. Haensch, W. et al. Silicon CMOS devices beyond scaling. *IBM J. Res. Dev.* **50**, 339–361 (2006).
2. Kanduri, A. et al. A perspective on dark silicon. In *The Dark Side of Silicon: Energy Efficient Computing in the Dark Silicon Era,* 3–20 (2017).
3. Zhang, Y. et al. Beyond conventional cooling: Advanced micro/nanostructures for managing extreme heat flux. *Adv. Mater.* **38**, e04706 (2026).
4. Swoboda, T. et al. Nanoscale temperature sensing of electronic devices with calibrated scanning thermal microscopy. *Nanoscale* **15**, 7139–7146 (2023).
5. Zhu, C., Bamidele, E. A., Shen, X., Zhu, G. & Li, B. Machine learning aided design and optimization of thermal metamaterials. *Chem. Rev.* **124**, 4258–4331 (2024).
6. Beardo, A. et al. Nanoscale confinement of phonon flow and heat transport. *npj Comput. Mater.* **11**, 172 (2025).

7. Chiritescu, C., Mortensen, C., Cahill, D. G., Johnson, D. & Zschack, P. Lower limit to the lattice thermal conductivity of nanostructured Bi_2Te_3-based materials. *J. Appl. Phys.* **106,** 073503 (2009).
8. Qian, X., Zhou, J. & Chen, G. Phonon-engineered extreme thermal conductivity materials. *Nat. Mater.* **20**, 1188–1202 (2021).
9. Kang, J. S., Li, M., Wu, H., Nguyen, H. & Hu, Y. Experimental observation of high thermal conductivity in boron arsenide. *Science* **361**, 575–578 (2018).
10. Mahan, G. D. Thermal transport in superlattices. *Phys. Rev. B-Condens. Matter Mater. Phys.* **83**, 125313 (2011).
11. Guo, Y. et al. Thermal conductivity minimum of graded superlattices due to phonon localization. *APL Mater.* **9**, 091104 (2021).
12. Cheaito, R. et al. Interplay between total thickness and period thickness in the phonon thermal conductivity of superlattices from the nanoscale to the microscale: Coherent versus incoherent phonon transport. *Phys. Rev. B.* **97**, 085306 (2018).
13. Zhang, Y. et al. On-chip high speed localized cooling using superlattice microrefrigerators. *IEEE Trans. Compon. Packag. Manuf. Technol.* **29**, 395–401 (2006).
14. Hijazi, M. & Kazan, M. Phonon heat transport in superlattices: Case of Si/SiGe and SiGe/SiGe superlattices. *AIP Adv.* **6**, 065024 (2016).
15. Graziosi, P. et al. Epitaxial SiGeSn alloys for CMOS-compatible thermoelectric devices. *ACS Appl. Energy Mater.* **13**, 9075–9082 (2025).
16. Li, W., Huang, X. & Ni, Y. Synergistic effects of phonon Anderson localization and resonance in Si/Ge superlattice nanowires: Toward lower thermal conductivity. *J. Phys. Chem. C.* **129**, 19093–19099 (2025).
17. Maranets, T. & Wang, Y. How phonon coherence develops and contributes to heat conduction in periodic and aperiodic superlattices. *Int. J. Therm. Sci.* **217**, 110018 (2025).
18. Wang, Y., Huang, H. & Ruan, X. Decomposition of coherent and incoherent phonon conduction in superlattices and random multilayers. *Phys. Rev. B.* **90**, 165406 (2014).
19. Luo, Y., Li, M., Yuan, H., Liu, H. & Fang, Y. Predicting lattice thermal conductivity via machine learning: A mini review. *npj Comput. Mater.* **9**, 4 (2023).
20. Cai, J., Chu, X., Xu, K., Li, H. & Wei, J. Machine learning-driven new material discovery. *Nanoscale Adv.* **2**, 3115–3130 (2020).
21. Chakraborty, P. et al. Quenching thermal transport in aperiodic superlattices: A molecular dynamics and machine learning study. *ACS Appl. Mater. Interfaces* **12**, 8795–8804 (2020).
22. Hu, R. et al. Machine-learning-optimized aperiodic superlattice minimizes coherent phonon heat conduction. *Phys. Rev. X.* **10**, 021050 (2020).
23. Chowdhury, P. R. & Ruan, X. Unexpected thermal conductivity enhancement in aperiodic superlattices discovered using active machine learning. *npj Comput. Mater.* **8**, 12 (2022).
24. Ding, W., Guo, J., An, M., Tsuda, K. & Shiomi, J. Human–AI collaboration for modeling heat conduction in nanostructures. *npj Comput. Mater.* **11**, 158 (2025).
25. Arabha, S., Aghbolagh, Z. S., Ghorbani, K., Hatam-Lee, S. M. & Rajabpour, A. Recent advances in lattice thermal conductivity calculation using machine-learning interatomic potentials. *J. Appl. Phys.* **130**, 210903 (2021).
26. Zhou, H., Ong, Z.-Y., Zhang, G. & Zhang, Y.-W. Computational predictions of quantum thermal transport across nanoscale interfaces. *Nanoscale* **14**, 9209–9217 (2022).
27. Ju, S., Shimizu, S. & Shiomi, J. Designing thermal functional materials by coupling thermal transport calculations and machine learning. *J. Appl. Phys.* **128**, 161102 (2020).
28. Kim, M., Hashemi, P. & Hoyt, J. L. Increased critical thickness for high Ge-content strained SiGe-on-Si using selective epitaxial growth. *Appl. Phys. Lett.* **97**, 262106 (2010).
29. Liu, X. et al. 200-period $(Si/Si_{0.8}Ge_{0.2}$ superlattice structure growth and characterization for vertical stacked DRAM. *Appl. Phys. Lett.* **126**, 232101 (2025).
30. Tian, Z., Esfarjani, K. & Chen, G. Green's function studies of phonon transport across Si/Ge superlattices. *Phys. Rev. B.* **89**, 235307 (2014).
31. Guo, Y. et al. Anharmonic phonon-phonon scattering at the interface between two solids by nonequilibrium Green's function formalism. *Phys. Rev. B.* **103**, 174306 (2021).
32. Lin, K.-H. & Strachan, A. Thermal transport in SiGe superlattice thin films and nanowires: Effects of specimen and periodic lengths. *Phys. Rev. B.* **87**, 115302 (2013).
33. Mu, X. et al. Ultra-low thermal conductivity in Si/Ge hierarchical superlattice nanowire. *Sci. Rep.* **5**, 16697 (2015).
34. Ran, X., Guo, Y., Hu, Z. & Wang, M. Interfacial phonon transport through Si/Ge multilayer film using Monte Carlo scheme with spectral transmissivity. *Front. Energy Res.* **6**, 28 (2018).
35. Larsen, A. N. Defects in epitaxial SiGe-alloy layers. *Mater. Sci. Eng. B.* **71**, 6–13 (2000).
36. Ulyanenkova, T. et al. Characterization of SiGe thin films using a laboratory X-ray instrument. *Appl. Crystallogr.* **46**, 898–902 (2013).
37. Deng, X. et al. Silicon epitaxy on h-terminated Si (100) surfaces at 250 °C. *Appl. Surf. Sci.* **378**, 301–307 (2016).
38. Ye, H. & Yu, J. Germanium epitaxy on silicon. *Sci. Technol. Adv. Mater.* **15**, 024601 (2014).
39. Norris, D. J. & Walther, T. Stranski–Krastanov growth of (Si) Ge/Si (001): Transmission electron microscopy compared with segregation theory. *Mater. Sci. Technol.* **34**, 1539–1548 (2018).
40. Chu, C.-L. et al. Ge/Si multilayer epitaxy and removal of dislocations from Ge-nanosheet-channel MOSFETs. *Sci. Rep.* **12**, 959 (2022).
41. Wedler, G., Walz, J., Hesjedal, T., Chilla, E. & Koch, R. Intrinsic stress upon Stranski–Krastanov growth of Ge on Si (001). *Surf. Sci.* **402**, 290–294 (1998).
42. Hu, M. & Poulikakos, D. Si/Ge superlattice nanowires with ultralow thermal conductivity. *Nano Lett.* **12**, 5487–5494 (2012).
43. Suda, Y., Hosoya, N. & Miki, K. Si submonolayer and monolayer digital growth operation techniques using Si_2H_6 as atomically controlled growth nanotechnology. *Appl. Surf. Sci.* **216**, 424–430 (2003).
44. Giannozzi, P. et al. QUANTUM ESPRESSO: A modular and open-source software project for quantum simulations of materials. *J. Phys. Condens. Mater.* **21**, 395502 (2006).
45. Togo, A. & Tanaka, I. First principles phonon calculations in materials science. *Scr. Mater.* **108**, 1–5 (2015).
46. Zhang, W., Fisher, T. S. & Mingo, N. Simulation of interfacial phonon transport in Si–Ge heterostructures using an atomistic Green's function method. *J. Heat. Transf.* **129**, 483–491 (2007).
47. Guo, Y. et al. Quantum mechanical modeling of anharmonic phonon-phonon scattering in nanostructures. *Phys. Rev. B.* **102**, 195412 (2020).
48. Guinea, F., Tejedor, C., Flores, F. & Louis, E. Effective two-dimensional hamiltonian at surfaces. *Phys. Rev. B.* **28**, 4397 (1983).
49. Wang, J.-S., Wang, J. & Lü, J. T. Quantum thermal transport in nanostructures. *Eur. Phys. J. B.* **62**, 381–404 (2008).
50. Mingo, N. & Yang, L. Phonon transport in nanowires coated with an amorphous material: An atomistic Green's function approach. *Phys. Rev. B.* **68**, 245406 (2003).
51. Rhyner, R. & Luisier, M. Atomistic modeling of coupled electron-phonon transport in nanowire transistors. *Phys. Rev. B.* **89**, 235311 (2014).
52. Murphy, N. C., Wortis, R. & Atkinson, W. A. Generalized inverse participation ratio as a possible measure of localization for interacting systems. *Phys. Rev. B.* **83**, 184206 (2011).
53. Bengio, Y., Goodfellow, I. & Courville, A. Deep learning, vol. 1 (MIT Press, Cambridge, MA, USA, 2017).

Acknowledgements

This work was supported by the COCONUT project from ANR (ANR-24-CE50-5682), AEI (Spain) [PID2022-141623NB-I00], Xunta de Galicia [ED431C-2022/016, ED431G-2023/04], and the European Union (ERDF/EU). The funders had no role in study design, data collection and analysis, decision to publish, or preparation of the manuscript. The Centre de Calcul

Intensif d'Aix-Marseille and CINES's Adastra are acknowledged for granting access to its high-performance computing resources. These authors contributed equally: Shubham Tyagi and Julian G. Fernandez.

Author contributions

S.T and M.B conceived the idea and coordinated the study. S.T and A.S performed and analyzed the DFT and NEGF simulations under the supervision of M.B. S.T, J.G.F, and N.S prepared the ML framework; carried out data analysis under the supervision of M.B and A.G.L.S.T, J.G.F, A.G.L, and M.B wrote the manuscript with inputs from all authors. M.B acquired the main funding for the study and supervised the project. All the authors discussed the results and reviewed the manuscript.

Competing interests

The authors declare no competing interests.

Additional information

Correspondence and requests for materials should be addressed to Shubham Tyagi or Marc Bescond.